Petroleum Science 23 (2026) 3587–3601

Contents lists available at ScienceDirect

Petroleum Science

journal homepage: www.keaipublishing.com/en/journals/petroleum-science

Original Paper

Conquering high-temperature acidic corrosion with a molecular anvil: A robust pyridinium quaternary ammonium salt

Hui-Ling Su, Zhi-Kun Wang *, Lei Yu, Xu-Peng Li, Jia-Qi Feng, Shi-Dong Xia, Zi-Xiao Chen, Mian-Tuo Li, Si-Yu Liu, Yu Fu, Jing-Yue Wang, Song-Qing Hu **

Shandong Key Laboratory of Intelligent Energy Materials, School of Materials Science and Engineering, China University of Petroleum (East China), Qingdao, 266580, Shandong, China

ARTICLE INFO

Article history:
Received 17 December 2025
Received in revised form
10 March 2026
Accepted 11 March 2026
Available online 14 March 2026

Edited by Yan-Hua Sun

Keywords:
Quaternary ammonium
Long alkyl chains
High temperatures
Strong acid
Corrosion protection

ABSTRACT

Achieving robust corrosion protection under extreme acidic and high-temperature conditions remains a formidable challenge in the oil and gas industry. In this work, we report a molecularly engineered corrosion inhibitor—a long-carbon-chain-functionalized quaternized pyridine derivative (Q4-AP-C12)—that has exceptional protection for N80 steel in highly aggressive environments at 500 mg/L. The inhibitor achieves corrosion rates of 0.029 g/(m^2·h) (99.86% inhibition efficiency) in 1 mol/L (3.6%) HCl solution at 303 K and 7.29 g/(m^2·h) (99.21% inhibition efficiency) in 15% HCl solution at 363 K. The superior performance is attributed to a rationally designed synergistic mechanism. X-ray photoelectron spectroscopy (XPS) and density functional theory (DFT) analyses confirm co-adsorption through electrostatic interaction of the quaternary ammonium group (N^+ peak at 402.5 eV) and chemical coordination via the pyridinic nitrogen (N–Fe peak at 399.8 eV), while the dodecyl chain enhances electron-donating ability (elevated HOMO energy at −7.57 eV) and strengthens interfacial adhesion (adsorption energy of −2.62 eV). At the morphological level, all-atom molecular dynamics (MD) simulations reveal that the alkyl chain drives the spontaneous self-assembly of a highly compact and stable bilayer film on the steel surface. This structured film significantly reduces surface roughness to 0.54 μm under aggressive conditions and acts as an effective hydrophobic barrier against corrosive species. By correlating macro-scale performance with atomic-scale interactions, this study provides deep molecular-level insights into the multi-mode adsorption and film formation, offering a robust strategy for designing high-performance inhibitors for demanding oilfield environments.

1. Introduction

Metallic infrastructure in petroleum engineering is frequently exposed to highly acidic and high-temperature environments, particularly during acid fracturing, downhole acidizing, and the transportation of sour hydrocarbons. These aggressive conditions precipitate severe corrosion, leading to rapid material degradation, operational disruptions, and catastrophic economic losses (Cui et al., 2023; Han et al., 2022; Liu et al., 2023a). Under such extreme regimes—characterized by elevated thermal energy and high proton concentrations—the application of effective corrosion inhibitors is essential yet remains a formidable challenge (Alawi Al-Sodani et al., 2018; Madurani et al., 2024). Although conventional organic inhibitors can form protective adsorbed layers, their efficacy often diminishes markedly under these conditions. High temperatures not only intensify corrosion kinetics but also accelerate inhibitor desorption (Meng et al., 2021; Wang et al., 2026), while high acidity promotes competitive adsorption by protons that displace the protective inhibitor species. Consequently, developing novel inhibitors capable of maintaining robust adsorption and film stability remains a critical priority for oil and gas field protection (Li et al., 2023).

To address these limitations, recent research has pivoted toward rational molecular design strategies (Ren et al., 2022; Saddik et al., 2025; Sun et al., 2025; Ye et al., 2019). Among these, the

* Corresponding author.
** Corresponding author.
E-mail addresses: wangzhikun@upc.edu.cn (Z.-K. Wang), songqinghu@upc.edu.cn (S.-Q. Hu).

Peer review under the responsibility of China University of Petroleum (Beijing).

https://doi.org/10.1016/j.petsci.2026.03.024

incorporation of long alkyl chains has emerged as an exceptionally effective approach (Edwards et al., 1994; Jia et al., 2024; Liu et al., 2023b; Moselhy et al., 2022; Singh et al., 2024; Zhao et al., 2024). Such structural modifications bolster interfacial hydrophobicity, drive spontaneous self-assembly on metal surfaces, and enhance the compactness of the resulting protective films. For instance, Fan et al. (2025) reported that a Mannich-base imidazoline quaternary ammonium salt modified with a C_{17} chain achieved over 98.7% inhibition efficiency (IE) in methyl sulfonic acid at 353 K. Similarly, Liu et al. (2022) developed SiO_2@OBQA composites by grafting a C_7 alkyl quaternary ammonium salt onto silica, which significantly mitigated the corrosion rate in 20% HCl solution at 180 °C. These advancements underscore the potential of integrating strong anchoring groups with hydrophobic structural units to forge high-performance inhibitors.

Complementary to hydrophobic tail modification, advanced inhibitor design also focuses on engineering polar headgroups to strengthen the primary adsorption bond (Haque et al., 2020; Tang et al., 2023). This strategy seeks to enhance chemisorption by introducing heterocyclic structures or functional groups with high electron density, facilitating the formation of stable coordinate covalent bonds with the metal surface. Heterocycles such as imidazole and pyridine, alongside multidentate groups like carboxylates and phosphonates, have been extensively explored (Liu et al., 2024; Gadioli et al., 2024; Luo et al., 2025; Marinescu, 2019; Verma et al., 2020, 2025; Wang et al., 2023, 2024). Furthermore, structural refinements—such as quaternization to introduce permanent positive charges for enhanced electrostatic attraction or the addition of electron-donating substituents—have been shown to substantially improve adsorption stability on the substrate (Goni et al., 2024; Jala et al., 2022; Lin et al., 2024; Tang et al., 2025; Zhang et al., 2023).

Guided by these principles, we report the synthesis of a novel long-carbon-chain-functionalized quaternized pyridine derivative (Q4-AP-C12), which synergistically combines robust adsorption motifs with a hydrophobic barrier unit. Prepared via a two-step process starting from 4-aminopyridine, the molecular structure of Q4-AP-C12 is designed to optimize protection: the pyridine ring and amino group serve as chemisorption sites for coordination bonding, the quaternary ammonium cation facilitates rapid electrostatic anchoring, and the dodecyl (C_{12}) chain drives the self-assembly of a dense hydrophobic barrier. The structure–activity relationship underlying the superior corrosion resistance of this molecule under harsh conditions is systematically explored and visually summarized in Fig. 1.

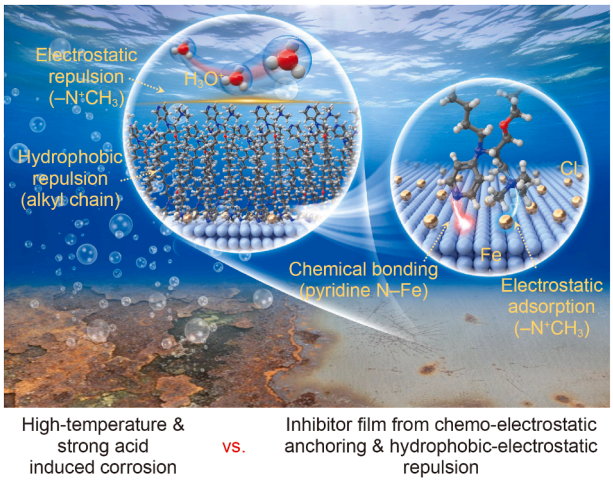

Fig. 1. Schematic diagram of the structure–activity relationship between the molecular structure and anti-corrosion performance of Q4-AP-C12.

2. Experiments and methods

2.1. Synthesis and characterization of Q4-AP and Q4-AP-C12

The intermediate Q4-AP was synthesized through nucleophilic ring-opening reaction between 4-AP and EPTAC at a 1:1 molar ratio. Specifically, 1 g (0.01 mol) of 4-AP was dissolved in 20 mL of isopropanol under ultrasonication. Then, 10 mL of an isopropanol solution containing 1.52 g (0.01 mol) of EPTAC was added dropwise. The reaction was carried out at 90 °C for 10 h under reflex, during which the solution color turned from clear and colorless to brown. After completion, the solvent was removed under reduced pressure using a rotary evaporator. The crude product was washed repeatedly with anhydrous ethanol to yield purified Q4-AP in 86.54% yield.

Q4-AP-C12 was then synthesized through nucleophilic substitution reaction between Q4-AP and $C_{12}H_{25}Br$. Typically, 1.46 g (0.01 mol) of Q4-AP and 4.98 g (0.02 mol) of $C_{12}H_{25}Br$ were dissolved in 20 mL of acetonitrile. The reaction proceeded at 90 °C for 24 h under continuous stirring. The product was precipitated by dropwise addition of the mixture into cold diethyl ether, collected by filtration, and washed three times with fresh diethyl ether to obtain pure Q4-AP-C12 in 82.23% yield.

The chemical structure of Q4-AP-C12 was characterized by Fourier transform infrared spectroscopy (FT-IR, Nicolet iS50) and nuclear magnetic resonance spectroscopy (^{1}H NMR, AVANCE NEO 600 MHz). Surface charge properties were determined using a nanoparticle size and zeta potential analyzer (SZ-100), and thermal stability was assessed via thermogravimetric analysis (TGA, STA8122).

2.2. Evaluation of corrosion inhibition performance

The corrosion inhibition performance of Q4-AP and Q4-AP-C12 was evaluated using weight loss measurements and electrochemical techniques. Prior to testing, N80 steel sheets (10 mm × 50 mm × 2 mm) were sequentially cleaned with acetone and ethanol, dried and weighed. The pre-treated N80 steel sheets were immersed in HCl solutions (1 mol/L and 15% HCl containing different concentrations of the inhibitors at 303 and 363 K, resulting in four distinct corrosive environments: 1 mol/L HCl (i.e. 3.6% HCl) at 303 and 363 K, 15% HCl at 303 and 363 K. After 4 h of immersion, the samples were ultrasonically washed in a rust removal solution, rinsed with ethanol, dried, and reweighed. The corrosion rate (C_R) was calculated by the following (Luo et al., 2024):

$$C_R = \frac{10^6(m - m_t)}{S \times t} \quad (1)$$

where C_R is the correction rate, g/(m^2·h); m and m_t are the initial and final mass of the sample, respectively, g; S is the total surface area, cm^2; t is the test time, h.

The inhibition efficiency (IE, %) was calculated by the following (Qian et al., 2019):

$$IE = \frac{C_R - C_{R(inh)}}{C_R} \times 100\% \quad (2)$$

where C_R and $C_{R(inh)}$ correspond to the corrosion rates in the absence and presence of the inhibitor, respectively.

Electrochemical measurements were conducted using a CHI760E electrochemical workstation. Before each test, the open

circuit potential (OCP) was stabilized by immersing the working electrode in the test solution for 30 min. Electrochemical impedance spectroscopy (EIS) was conducted at the OCP over a frequency range of 10^{-2} to 10^{5} Hz with a 5 mV amplitude perturbation. The resulting spectra were fitted to an appropriate equivalent circuit model using Zview software. Potentiodynamic polarization curves were recorded by scanning the potential from −500 to +500 mV relative to the OCP at a sweep rate of 0.2 mV/s. The corrosion potential (E_{corr}) and corrosion current density (i_{corr}) were determined via Tafel extrapolation of the polarization curves.

The morphologies of the corroded steel surfaces were examined using scanning electron microscopy (SEM, FEI). The SEM imaging was conducted at an acceleration voltage of 10 kV to optimize the topographic contrast and resolution. A 3D ultra-depth-of-field digital microscope (SDM, DSX1000) was also used to characterize the topographic features and surface roughness. Surface wettability was characterized by contact angle measurements (JC2000D) to evaluate the hydrophobicity imparted by inhibitor adsorption. Furthermore, the elemental composition and states on the steel surface were analyzed by X-ray photoelectron spectroscopy (XPS, Nexsa).

2.3. Computational methods

The molecular reactivity and adsorption behavior of Q4-AP and Q4-AP-C12 on iron surface were investigated by density functional theory (DFT) calculations using the Materials Studio software. The generalized gradient approximation (GGA) with the Perdew-Burke-Ernzerhof (PBE) functional was employed. The system was treated with spin unrestricted settings, and the total charge was set to +1. Geometry optimization was performed with the following convergence tolerances: energy change of 1.0×10^{-5} Ha, maximum force of 0.002 Ha/Å, and maximum displacement of 0.005 Å. A *k*-point grid of 3 × 3 × 1 was used for Brillouin zone sampling. Core electrons were treated with DFT semi-core pseudopotentials, and the double numerical plus polarization (DNP) basis set (version 4.4) was adopted. The self-consistent field (SCF) convergence tolerance was set to 1.0×10^{-6}. For charge and spin density mixing, mixing parameters of 0.2 and 0.5 were applied, respectively. To accelerate SCF convergence, the direct inversion in the iterative subspace (DIIS) method was employed with a size of 10. The charge density preconditioner was enabled with a damping parameter $q_0 = 20$ to suppress charge density oscillations. Additionally, a thermal smearing value of 0.006 Ha was applied to the orbital occupation to facilitate convergence.

All-atom molecular dynamics (MD) simulations were performed to investigate the adsorption kinetics of corrosion inhibitor film on iron surface in a HCl solution. A Fe (110) surface with dimensions of 36.48 Å × 37.26 Å was constructed, consisting of six atomic layers. The solution phase contains 2500 H_2O, along with 45 H_3O^+ and 45 Cl^- ions to mimic 1 mol/L HCl solution, and 211 H_3O^+ and 211 Cl^- ions to mimic 15% HCl environments. 5, 15, 25, or 35 Q4-AP-C12 molecules were introduced into the solution. The number of Cl^- was adjusted accordingly to maintain overall charge neutrality. A vacuum layer of 100 Å was added above the solution phase to eliminate spurious interactions in the *z*-direction. To simulate the effect of adsorbed chloride ions on surface charge, 20% of the chloride ions in solution were randomly pre-adsorbed onto the Fe surface. The surface was fixed during all simulations. Periodic boundary conditions were applied in all three directions.

The COMPASSII force field was employed. Electrostatic and van der Waals interactions were treated using the Ewald and Atom-based (cutoff 12.5 Å) summation methods, respectively. Subsequently, NVT ensemble simulations were conducted at either 303 or 363 K using the Nosé-Hoover-Langevin (NHL) thermostat. The integration time step was set to 1.0 fs, and trajectories were saved every 2000 steps for analysis. The total simulation time ranged from 2 to 4 ns, depending on the specific system, to ensure adequate equilibration. Trajectory analysis was performed using in-house Perl scripts to extract relevant adsorption and structural properties.

3. Results and discussion

3.1. Synthesis and structural characterization of Q4-AP-C12

The structures of the target corrosion inhibitor Q4-AP-C12 and its intermediate Q4-AP were investigated using spectroscopic and physicochemical characterization (Fig. 2). In the FT-IR spectrum (Fig. 2(b)), the successful quaternization of 4-AP is evidenced by the emergence of a characteristic methyl bending vibration at 1478 cm^{-1}, accompanied by the concomitant disappearance of the primary amine stretching bands at 3437 and 3250 cm^{-1}. Following the grafting of the dodecyl chain, the aliphatic C–H stretching vibrations at 2930 and 2850 cm^{-1} are markedly intensified, reflecting the significantly increased density of methylene groups in the hydrophobic tail. Furthermore, the molecular structure was rigorously validated by ^1H NMR (Fig. 2(c)), where all observed signals (δ = 8.04–7.98 (2H), 6.89–6.82 (2H), 4.30–4.04 (4H), 3.94–3.67 (1H), 3.56–2.95 (H), 1.93–1.57 (4H), 1.49–1.00 (36H), and 0.77–0.68 (4H)) precisely correspond to the protons of Q4-AP-C12, confirming a high-purity product.

Zeta potential measurements (Fig. 2(d)) confirmed that both Q4-AP and Q4-AP-C12 maintain positive surface charges across a broad pH range, consistent with the presence of the quaternary ammonium (N^+) center. Notably, Q4-AP-C12 exhibits a significantly higher zeta potential at neutral pH (+71.9 mV at pH 7) compared to its precursor. This enhancement is attributed to the dodecyl chain promoting a more ordered solvation shell and reducing the shielding effect of counterions (Cl^-), thereby increasing the effective charge density (Pisárčik et al., 2021). This property is pivotal for strong electrostatic adsorption onto negatively charged metal surfaces, a prerequisite for the initial stage of the corrosion inhibition mechanism (Kokalj et al., 2022; Xhanari et al., 2025). TG analysis (Fig. 2(e)) demonstrates that the incorporation of the dodecyl chain substantially enhances thermal stability, a critical requirement for high-temperature oilfield applications. Whereas the hydrophilic Q4-AP exhibits significant moisture desorption (8.9% at 90 °C) and initiates decomposition at approximately ~240 °C, Q4-AP-C12 demonstrates minimal moisture loss (1.9% at 90 °C) and a significantly increased primary decomposition temperature of ~360 °C. This superior thermal resilience is ascribed to the enhanced molecular hydrophobicity and robust van der Waals-driven intermolecular associations, which synergistically bolster the structural integrity of the inhibitor against thermal degradation.

3.2. Gravimetric analysis of corrosion inhibition under high-temperature and strong acid conditions

The corrosion inhibition efficiencies of Q4-AP and Q4-AP-C12 were quantitatively assessed via weight loss measurements under demanding high-temperature and acidic conditions (Fig. 3). For both inhibitors, corrosion rates declined precipitously with increasing concentration before reaching a steady-state plateau, signifying the formation of a compact protective film on the metallic substrate.

Q4-AP demonstrates moderate efficiency under relatively mild conditions. In 1 mol/L HCl solution at 303 K, the corrosion rate was reduced from 20.39 (blank) to 1.96 g/(m^2·h) at a concentration of

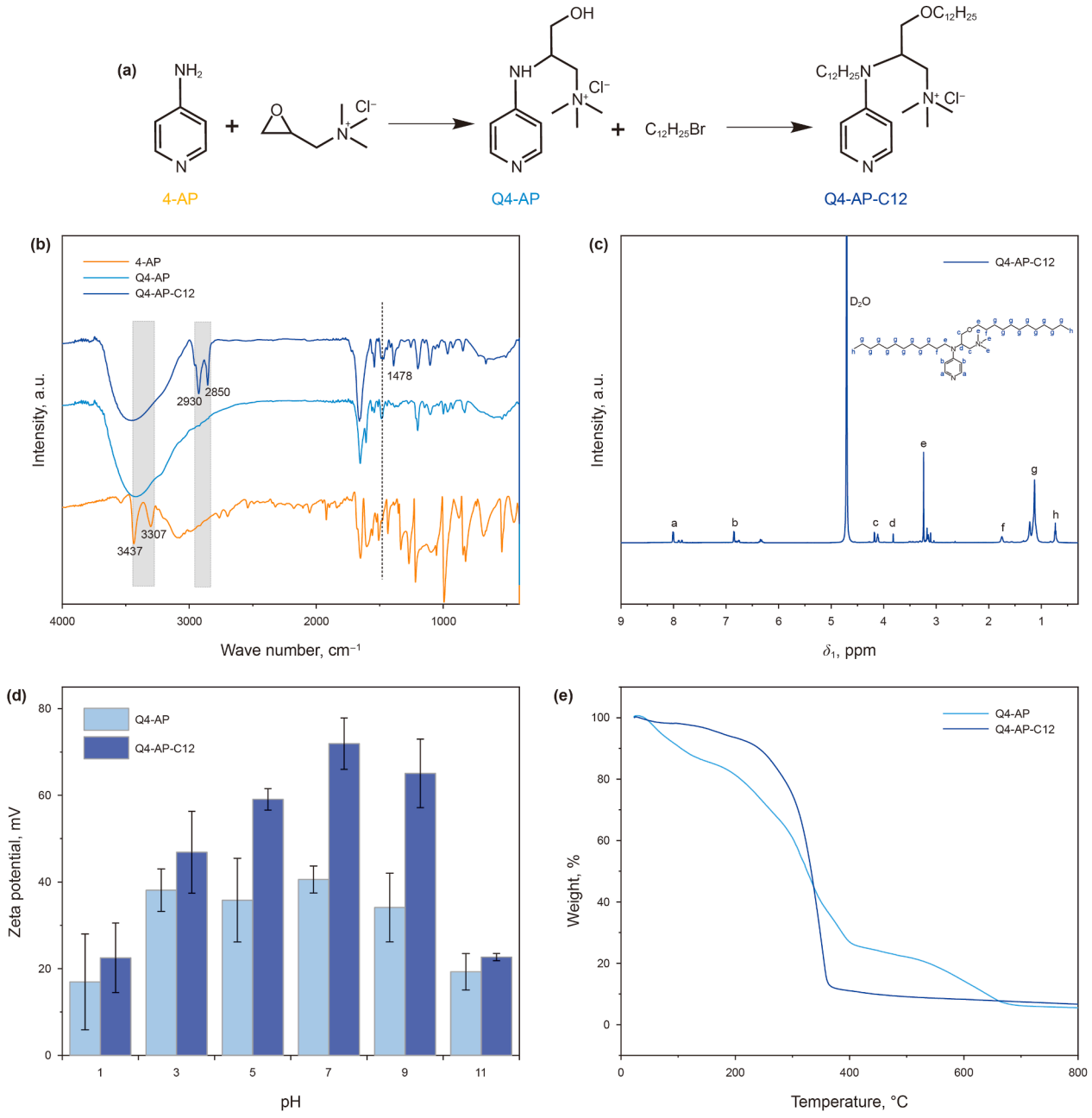

Fig. 2. Characterization of Q4-AP and Q4-AP-C12. (**a**) Reaction scheme; (**b**) IR spectra; (**c**) ^{1}H NMR spectrum; (**d**) zeta potentials; (**e**) TGA curves.

100 mg/L (90.35% efficiency). A performance plateau was established at approximately 200 mg/L, beyond which corrosion rates stabilized between 1.64 and 1.95 g/(m^2·h) (91%–92% efficiency). However, its protective capability diminishes markedly under more aggressive regimes. Specifically, in 15% HCl solution at 363 K, the corrosion rate only dropped to 422.14 g/(m^2·h) at 500 mg/L (54.24% efficiency). This performance failure is likely driven by the intense competitive adsorption of protons (H^+), which displaces inhibitor cations from the surface, coupled with the thermal and chemical destabilization of the adsorbed layer at elevated temperatures.

In contrast, Q4-AP-C12 exhibits exceptional inhibition across all experimental conditions. In 1 mol/L HCl solution at 303 K, it achieves a negligible corrosion rate of 0.029 g/(m^2·h) at 500 mg/L (99.86% efficiency), with near-optimal protection (98.83%) attained at concentrations as low as 10 mg/L. Critically, even under extreme conditions (15% HCl, 363 K), Q4-AP-C12 remains robust; at 200 mg/L, the corrosion rate is mitigated to 31.73 g/(m^2·h), further reaching 7.29 g/(m^2·h) (99.21%) at 500 mg/L. This remarkable performance is ascribed to the hydrophobic dodecyl chain, which facilitates the self-assembly of a dense interfacial barrier. This alkyl tail acts synergistically with the quaternary ammonium anchoring group to maintain a stable, high surface coverage even in highly aggressive oilfield environments.

3.3. Electrochemical analysis of corrosion behavior and inhibition mechanism

The corrosion inhibition mechanism of Q4-AP-C12 was comprehensively investigated using electrochemical impedance

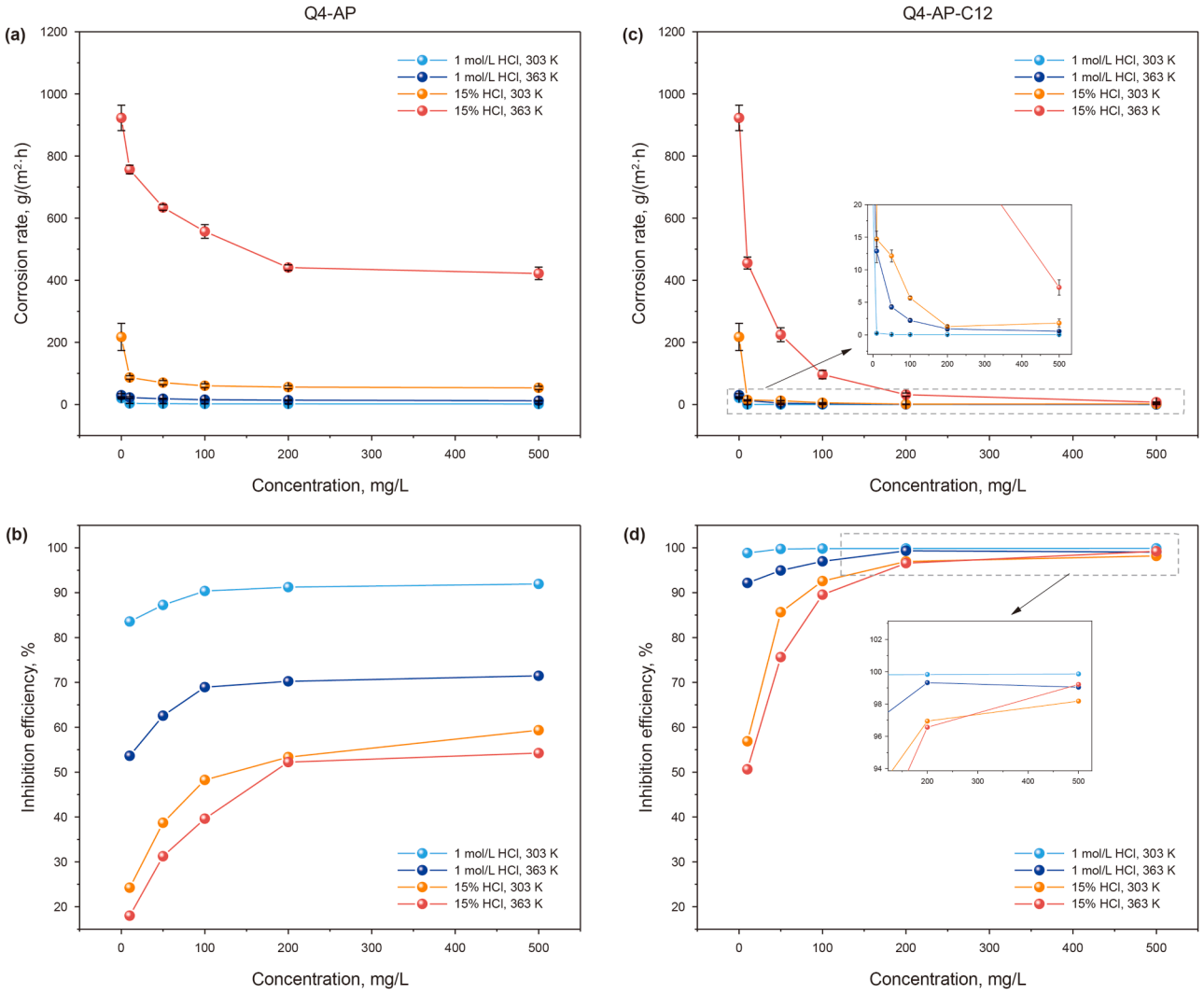

Fig. 3. Corrosion rates (**a**, **c**) and inhibition efficiencies (**b**, **d**) of Q4-AP and Q4-AP-C12 at various concentrations in 1 mol/L and 15% HCl solutions at 303 and 363 K, respectively.

spectroscopy (EIS) and potentiodynamic polarization (PDP). The extracted equivalent circuit parameters, including the constant phase element (CPE_{dl}), solution resistance (R_s), and charge transfer resistance (R_{ct}), are compiled in Table S1. The inhibition efficiency (*IE*) was calculated from the charge transfer resistance ($IE = (R_{ct} - R_{ct,0})/R_{ct} \times 100\%$) (Ansari et al., 2020), where R_{ct} and $R_{ct,0}$ represent the charge transfer resistances with and without the inhibitor, respectively.

As shown in Fig. 4(a, d, g, j), the Nyquist plots exhibit depressed capacitive loops, characteristic of a charge-transfer-controlled corrosion process. The fitted parameters reveal a substantial elevation in R_{ct} values with increasing inhibitor concentration. Specifically, in 15% HCl solution at 363 K, R_{ct} increases dramatically from 0.12 (blank) to 20.4 Ω·cm^2 (500 mg/L), corresponding to an exceptional inhibition efficiency of 99.41%. This significant enhancement in impedance corroborates the formation of a high-resistance adsorption film, which effectively impedes charge transfer at the metal–solution interface and mitigates corrosion susceptibility (Berdimurodov et al., 2022; Jamil et al., 2025; Li et al., 2025; Zhong et al., 2026).

Simultaneously, Bode plots (Fig. S1) display a marked increase in the low-frequency impedance modulus with higher inhibitor dosages, robustly supporting the establishment of a compact protective barrier. The presence of a single time constant across all spectra attests to the charge-transfer-controlled nature of the reaction. Furthermore, the phase angles broaden and increase in magnitude (Wang et al., 2022), providing further evidence that the adsorbed inhibitor layer effectively blocks the corrosion process. Comparable electrochemical behavior is observed for the intermediate Q4-AP (Fig. S2(a–d)). To ensure fitting accuracy, a constant phase element (CPE_{dl}) was utilized to replace the ideal double-layer capacitor in the equivalent circuit model depicted in Fig. 4(l).

Potentiodynamic polarization curves (Fig. 4(b, e, h, k)) provide corroborative evidence for the superior efficacy of Q4-AP-C12. Key electrochemical parameters, including corrosion current density (i_{corr}), corrosion potential (E_{corr}), and anodic/cathodic Tafel slopes (β_a, β_c), were derived via Tafel extrapolation (Table S2). The inhibition efficiency was calculated as follows: $\left(IE = \left(i^0_{corr} - i_{corr}\right)/i^0_{corr} \times 100\%\right)$, where i^0_{corr} and i_{corr} are the corrosion current densities without and with inhibitor, respectively. Across all aggressive environments assayed, i_{corr} exhibits a precipitous decline with increasing inhibitor dosage. For instance, at 500 mg/L, i_{corr} drops from 0.40 to 0.02 μA/cm^2 in 1 mol/L HCl solution (303 K), and notably from 61.66 to 0.79 μA/cm^2 even in 15% HCl solution at 363 K. The displacement in E_{corr} remains within ±85 mV relative to the

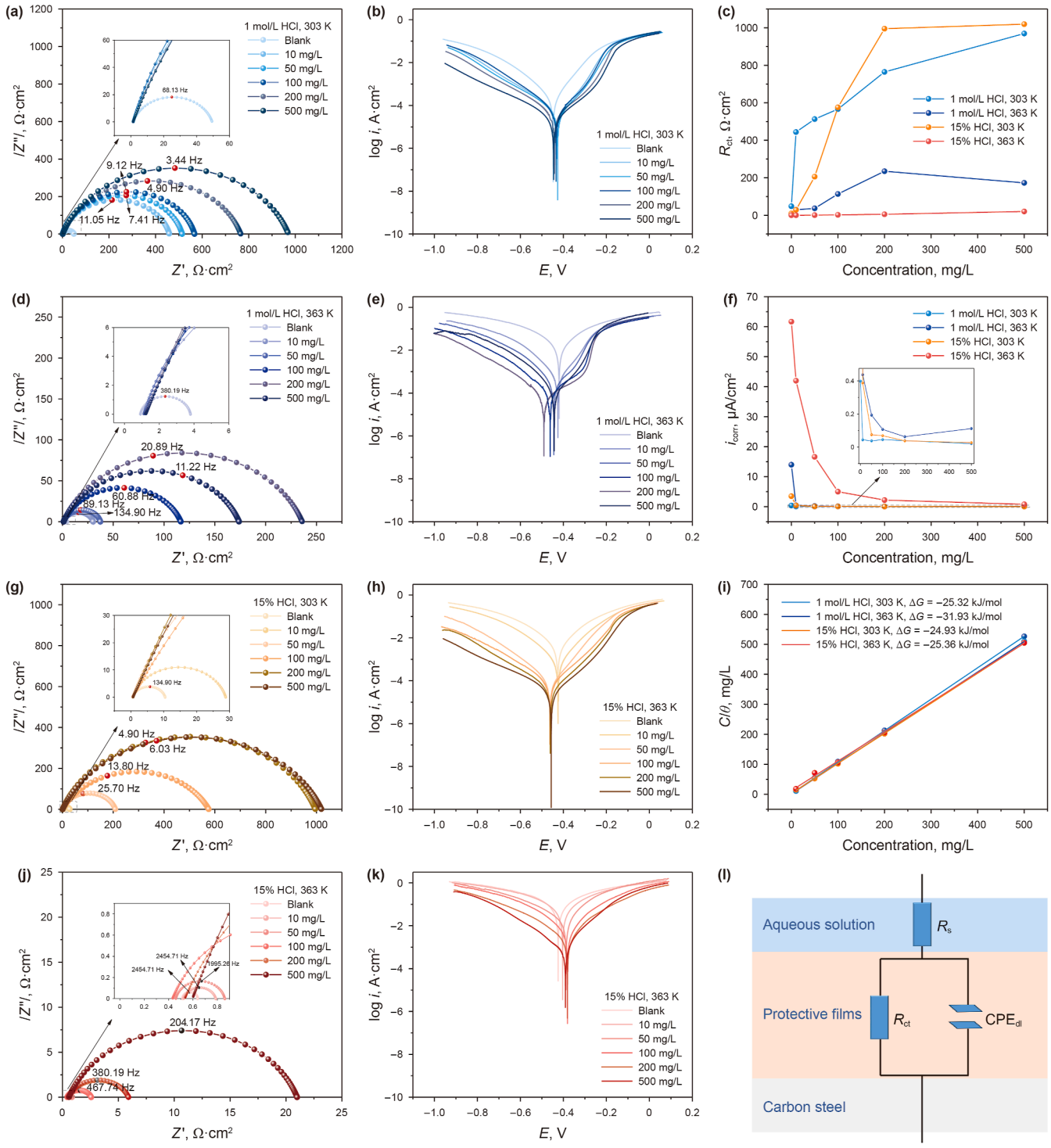

Fig. 4. Nyquist plots (**a**, **d**, **g**, **j**) and polarization curves (**b**, **e**, **h**, **k**). R_{ct} variation curves (**c**), i_{corr} variation curves (**f**), fitted adsorption isotherms (**i**) of Q4-AP-C12 at various concentrations in HCl solutions at 303 and 363 K, respectively, and equivalent circuit models (**l**).

blank under all conditions, classifying Q4-AP-C12 as a mixed-type inhibitor that concurrently suppresses both anodic metal dissolution and cathodic hydrogen evolution (Wazzan et al., 2022; Wen et al., 2023). Q4-AP exhibits similar mixed-type inhibition characteristics, as detailed in Fig. S2(e, f) and Tables S3 and S4.

To explain the surface interaction mechanism, the adsorption characteristics of Q4-AP-C12 were fitted to the Langmuir adsorption isotherm (Ahmadi et al., 2024; Zhang et al., 2023), as depicted in Fig. 4(i). The linear form of the isotherm is expressed as $\theta/(1-\theta) = K_{ads}C$, where θ is the surface coverage, K_{ads} is the adsorption equilibrium constant, and C is the inhibitor concentration. The high correlation coefficients ($R^2 > 0.99$) obtained from the linear regression plots under all four experimental conditions demonstrate a strong adherence to the Langmuir model, suggesting monolayer adsorption on the metal surface. Subsequently, the standard Gibbs free energy of adsorption (ΔG_{ads}) was calculated using the following equation: $\Delta G_{ads} = -RT\ln(1000K_{ads})$, where R is the gas constant (8.314 J/(mol·K)), T is the absolute temperature,

and the value 1000 accounts for the concentration of water in g/L. The calculated ΔG_{ads} values are −25.32, −31.93, −24.93, and −25.36 kJ/mol for 1 mol/L HCl at 303 K, 1 mol/L HCl at 363 K, 15% HCl at 303 K, and 15% HCl at 363 K, respectively. Generally, values strictly less negative than −20 kJ/mol indicate physisorption via electrostatic interactions, while those more negative than −40 kJ/mol signify chemisorption involving coordinate bond formation. The obtained values, falling within the range of −20 to −40 kJ/mol, suggest a comprehensive adsorption mode involving both physical and chemical mechanisms (mixed-type adsorption). These thermodynamic parameters confirm that Q4-AP-C12 spontaneously forms a stable and compact protective film on the N80 steel surface through robust interfacial interactions, thereby sustaining its exceptional inhibition performance even in highly aggressive environments. A similar mixed-mode adsorption mechanism is observed for the intermediate Q4-AP, as illustrated in Fig. S2(g, h).

3.4. Morphological characterization of surface protection and film stability

To further clarify the corrosion inhibition mechanism beyond electrochemical parameters, the interfacial stability and protective quality of the inhibitor films were investigated using morphological and wettability techniques. Scanning electron microscopy (SEM) analysis (Fig. 5) provides direct visual evidence of the interfacial phenomena. The severe surface deterioration observed in the blank experiments underscores the aggressive nature of the corrosive media. In contrast, the steel surface protected by 500 mg/L Q4-AP-C12 exhibits markedly mitigated damage. Under milder conditions (1 mol/L HCl solution at 303 and 363 K and 15% HCl solution at 303 K), the original polishing abrasions remain clearly visible, attesting to the exceptional integrity of the protective barrier.

The distinct disparity in film quality between Q4-AP and Q4-AP-C12 is evident. The latter not only minimizes pit density but also preserves the microscopic smoothness of the substrate, suggesting the formation of a more coherent and defect-free adsorption layer. These qualitative observations are quantitatively corroborated by 3D surface topography analysis (Fig. S3). The arithmetic mean height of surface roughness (S_a) increases sharply for blank samples exposed to harsh conditions. However, the addition of inhibitors significantly reduces S_a values, with the Q4-AP-C12 formulation demonstrating the most pronounced smoothing effect. Notably, under the most aggressive condition (15% HCl solution, 363 K), the S_a value is substantially reduced from 11.02 (blank) to 3.37 μm (Q4-AP), and further to a mere 0.54 μm (Q4-AP-C12). This dramatic reduction confirms the construction of an exceptionally smooth and uniform protective film on the steel surface.

The systematic increase in contact angle correlates directly with the extent of surface passivation. The superior hydrophobicity observed for Q4-AP-C12 confirms the successful assembly of a well-ordered, hydrocarbon-rich alkyl layer. This structure creates a thermodynamic barrier against aqueous permeation, operating synergistically with the physical barrier identified in the morphological analysis (Lai et al., 2021; Liao et al., 2023). Collectively, these results provide compelling evidence that the exceptional efficacy of Q4-AP-C12 is derived from its ability to form a robust, multifunctional film. This film exhibits outstanding stability, preserving its protective integrity by suppressing both chemical dissolution (as evidenced by retained polishing marks) and physical roughening, thereby establishing a new benchmark for corrosion protection under extreme conditions.

To investigate the dynamic stability and self-healing potential of the inhibitor film, the aging behavior of N80 steel was monitored in 1 mol/L HCl solution at 363 K. The 3D topographic maps (Fig. 6(a, b)) and corresponding quantitative metrics (Fig. 6(c–e)) reveal fundamentally distinct degradation pathways for the unprotected and protected surfaces. The blank sample exhibits a trajectory of accelerated deterioration. The progressive increase in surface roughness (S_a increases from 0.58 to 2.69 μm) and the escalating corrosion rate (139.46 to 187.23 g/(m^2·h)) are characteristic of an unstable interface undergoing active, localized dissolution. Conversely, the Q4-AP-C12-protected interface demonstrates remarkable dynamic stability. The maintenance of consistently low roughness (S_a < 0.43 μm) and negligible corrosion rates (C_R < 5.45 g/(m^2·h)) over time suggests a mechanism beyond a simple static barrier. Instead, it implies the establishment of a dynamic adsorption–desorption equilibrium that may facilitate the self-repair of micro-defects, effectively arresting the initiation and propagation of localized corrosion. This temporal resilience corroborates earlier findings and highlights the significant potential of Q4-AP-C12 for long-term industrial applications.

3.5. Unraveling the interfacial adsorption by XPS analysis

To unravel the molecular interactions underlying the superior inhibition performance, a detailed XPS analysis of the steel/inhibitor interface was conducted under varying corrosion durations and aggressive media. In 1 mol/L HCl solution at 363 K, the survey spectra confirmed the presence of Fe, O, N, and C on the steel surface (Fig. 7(a)). High-resolution N 1*s* spectra at different exposure intervals (Fig. 7(b)) reveal that the surface nitrogen content surged to 3.43% within the first 5 min, followed by a gradual saturation. This trend suggests a rapid initial adsorption phase succeeded by the densification of the protective layer.

Furthermore, the deconvolution of N 1*s* spectra under four distinct corrosion conditions (Fig. 7(c)) resolved three characteristic peaks at 402.5 eV (N^+–C), 399.8 eV (N–Fe), and 397.8 eV (N–C), indicating a hybrid adsorption mechanism. The N^+–C component corroborates the electrostatic interaction of quaternary ammonium cations with the charged surface, whereas the peak at 399.8 eV provides compelling evidence of coordinative N–Fe bonding, signifying robust chemisorption. Complementing this, the C 1*s* spectrum (Fig. S4(a)) exhibits dominant signals at 284.8 eV (C–C/C–H), alongside contributions at 286.4 eV (C–N^+) and 288.5 eV (O–C=O). These features indicate a substantial interfacial enrichment of dodecyl chains. This pattern attests to the dense packing of hydrophobic tails, forming a hydrocarbon-rich barrier anchored by the strongly adsorbed headgroups.

The evolution of surface chemical states further substantiated the protective nature of the film. The Fe 2*p* spectra (Fig. S4(b)) were resolved into metallic Fe^0 (707.0 eV), Fe^{2+} (710.6 and 724.8 eV), and Fe^{3+} (712.6 and 728.5 eV) species. Notably, the detection of metallic Fe^0 was confined to mild conditions (1 mol/L HCl solution, 303 K), while the Fe^{3+} content increased markedly under harsher regimes (Table S5), reflecting enhanced oxidation. The Fe^{3+}/Fe^{2+} ratio serves as a spectroscopic indicator of corrosion severity, correlating directly with the extent of surface oxidation. A higher ratio implies a more thoroughly oxidized surface, consistent with the severe material degradation observed in the absence of effective protection.

Based on the cumulative experimental and theoretical evidence, the inhibition mechanism of Q4-AP-C12 is schematically illustrated in Fig. 7(d). In uninhibited, high-temperature acidic solutions, the steel substrate undergoes severe active dissolution, generating extensive pits and corrosion products. Upon the addition of Q4-AP-C12, corrosion is effectively mitigated through a

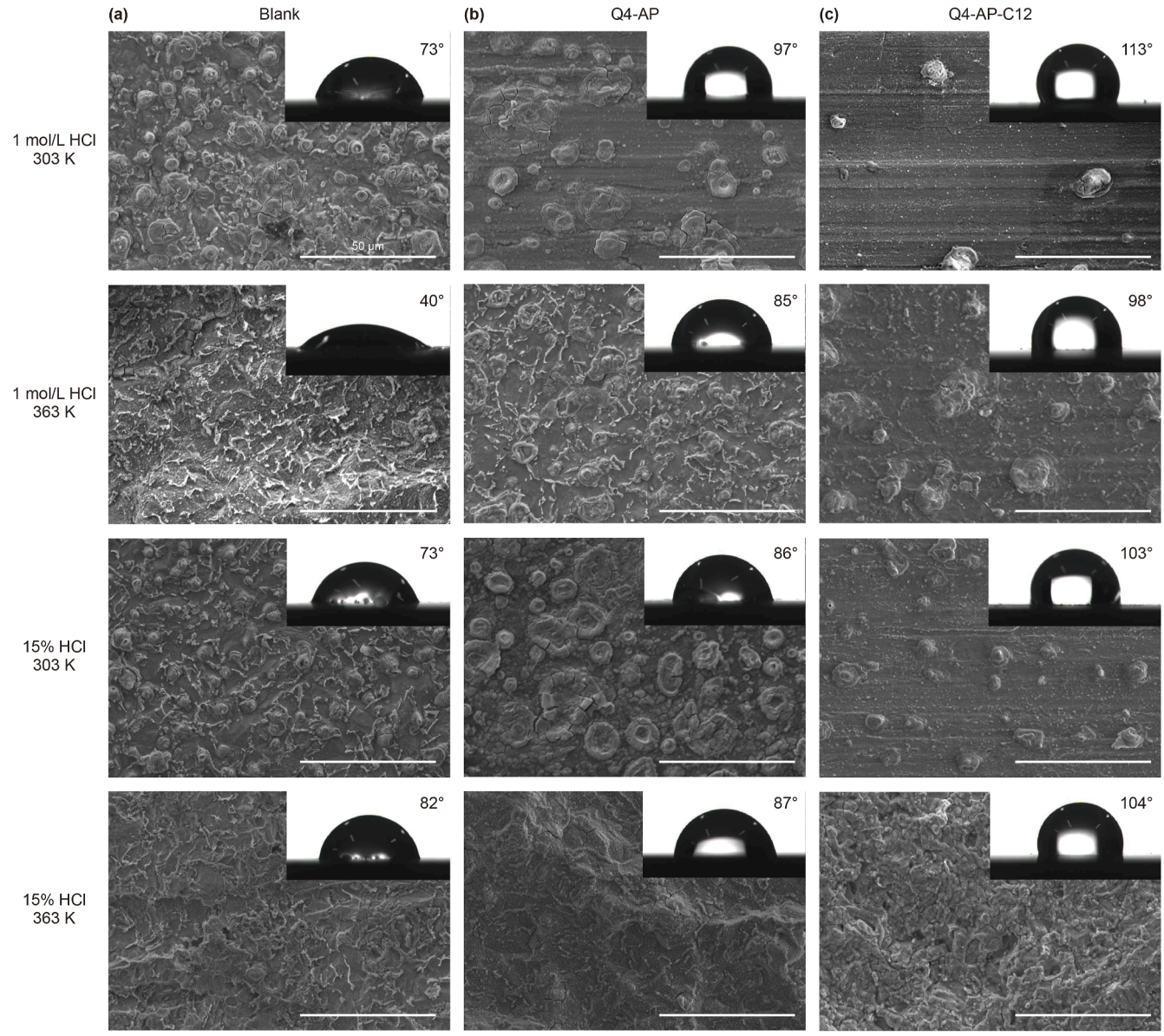

Fig. 5. Surface characterization (SEM and contact angle) comparing the protective effects of the blank (**a**), Q4-AP (**b**), and Q4-AP-C12 (**c**) inhibitors at 500 mg/L under different conditions after 4 h immersion.

synergistic tripartite mechanism: (1) chemisorption via the pyridine nitrogen, (2) physisorption driven by quaternary ammonium cations, and (3) the formation of a hydrophobic barrier by the long alkyl chains. This collaborative, multi-mode adsorption strategy underpins the excellent and durable performance of the inhibitor, even under extreme environmental conditions.

3.6. DFT modeling of electronic structure and surface interactions

Density functional theory (DFT) calculations were performed to understand the electronic origins of the superior inhibition performance of Q4-AP-C12 compared to Q4-AP on an iron surface (Fig. 8). The integrated computational results demonstrate that the incorporation of the dodecyl chain systematically fine-tunes the electronic properties, tailors local reactivity, and significantly enhances adsorption strength and interfacial charge transfer, confirming that Q4-AP-C12 exhibits superior corrosion inhibition performance due to optimized electronic interactions and strengthened adsorption with the Fe substrate. Frontier molecular orbital analysis (Fig. 8(a)) reveals that Q4-AP-C12 has a higher-energy highest occupied molecular orbital (HOMO, −7.57 eV) than Q4-AP (−7.91 eV), indicating a greater propensity to donate electrons to the metal surface, despite a slightly larger energy gap (4.17 vs. 4.02 eV). The relationship between the HOMO-LUMO energy gap (ΔE) and inhibition performance is nuanced. While Q4-AP-C12 has a slightly larger ΔE (4.17 vs. 4.02 eV for Q4-AP), which often correlates with higher kinetic stability and lower chemical reactivity, its significantly higher HOMO energy is the dominant factor facilitating stronger electron-donating interactions with the Fe surface. This combination—enhanced electron-donating ability coupled with sufficient molecular stability—is favorable for forming a robust and durable adsorbed layer. Fukui function analysis (Fig. 8(b–e)) shows a tailored local reactivity: key electrophilic sites (e.g., C2, C5) exhibit enhanced reactivity (increased f^{+}) in Q4-AP-C12, while the nucleophilic reactivity of the critical N3 atom decreases (f^{-}: from 0.25 to 0.108),

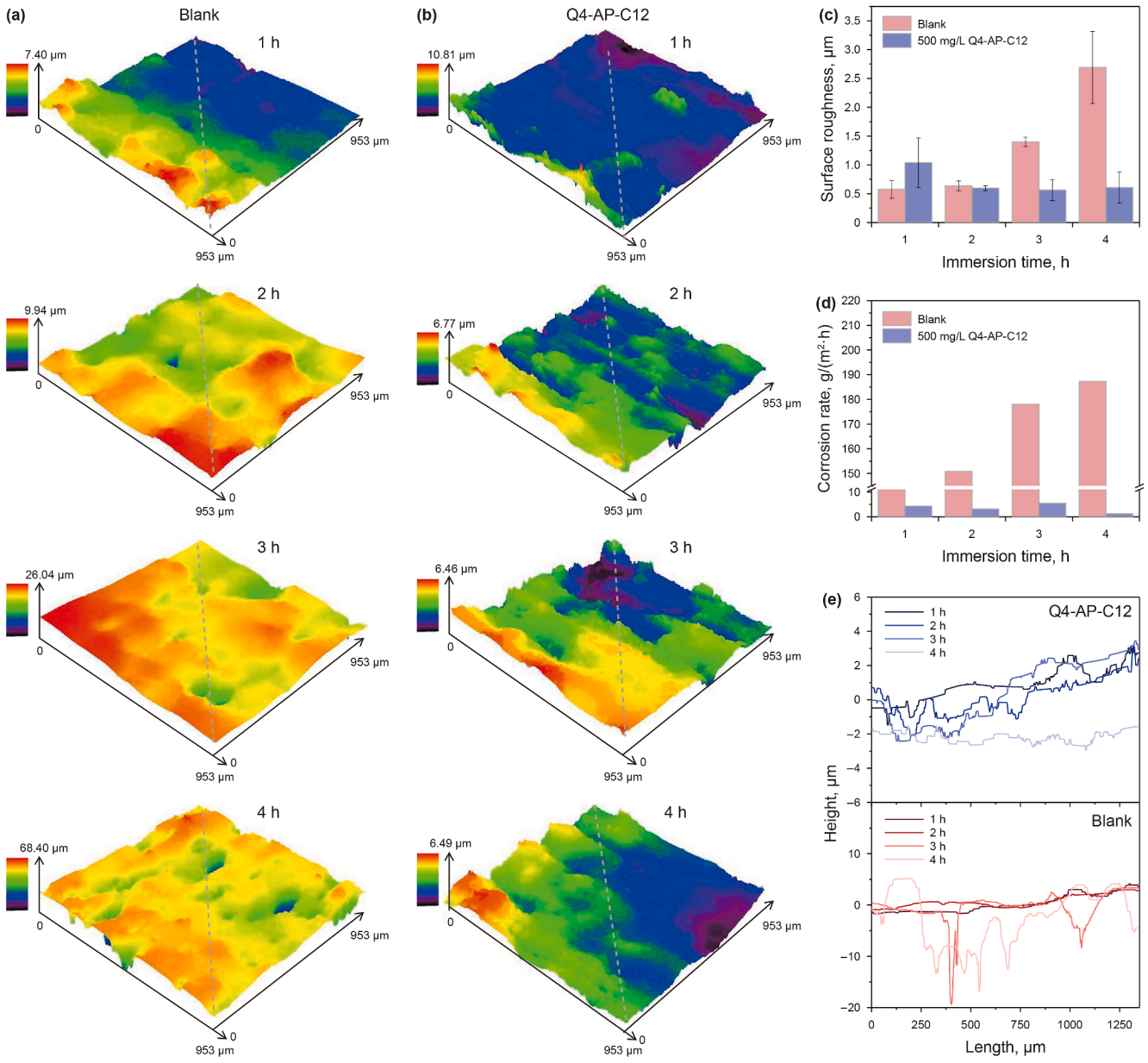

Fig. 6. Aging behavior of the corrosion inhibition film over time. (**a**, **b**) 3D surface topographies for the blank and 500 mg/L Q4-AP-C12 samples, respectively, after immersion in 1 mol/L HCl solution at 363 K for 1–4 h. (**c**) Surface roughness (S_a), (**d**) corrosion rate, and (**e**) mean line roughness are plotted as a function of immersion time.

and the etherified O15 shows reduced reactivity, reflecting the electronic modulation by the alkyl chain.

Electrostatic potential (ESP) mapping reveals a complementary alignment between the nucleophilic pyridinic nitrogen and electron-deficient regions on the Fe surface, which promots the formation of coordination bonds (Fig. 8(f, g)). The grafted C12 chain introduces a distinct region of higher ESP, which modulates the adsorption orientation and strengthens affinity. Crucially, differential charge density analysis confirms substantial electron transfer from the Fe surface to the pyridinic N, followed by redistribution along the pyridine ring toward the quaternary ammonium group (Fig. 8(h, i)). The distribution of interfacial electron transfer density (ρ) provides further insight into this process (Fig. 8(j)). Although the maximum electron densities for both inhibitors are comparable (~0.0048 e/Å^3) with similar spatial extents along the z-axis (span ≈ 2.38 Å), indicating that the carbon chain modification does not significantly alter the overall charge transfer magnitude or distribution, a critical difference emerges in the proximity of the functional groups. The Fe–N bond lengths are 2.112 and 2.130 Å for Q4-AP and Q4-AP-C12, respectively. More importantly, the quaternary ammonium group in Q4-AP-C12 is located notably closer to the Fe surface (4.299 vs. 4.683 Å in Q4-AP). This reduced distance corresponds to a shorter electron transfer initiation pathway for Q4-AP-C12, suggesting a more direct and efficient charge transfer mechanism that facilitates stronger adsorption of the functionalized inhibitor.

The computed adsorption energy of Q4-AP-C12 (−2.62 eV) is considerably more negative than that of Q4-AP (−1.84 eV), affirming stronger chemisorption (Fig. 8(k)). Density of states (DOS) analysis (Fig. 8(l)) provides additional evidence. The adsorption of both molecules broadens the total DOS of the Fe surface, with the Fe + Q4-AP-C12 system exhibiting higher

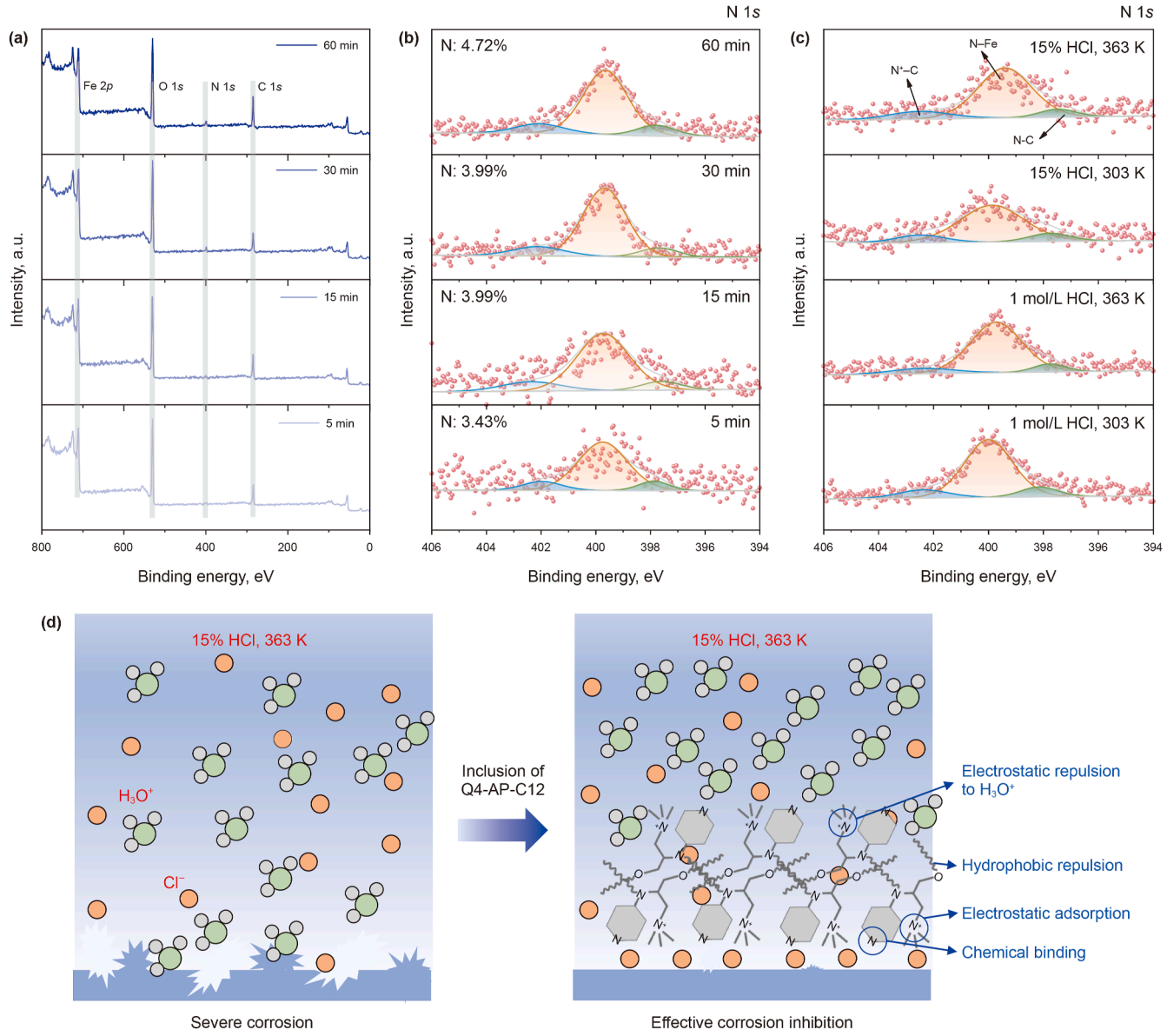

Fig. 7. (**a**, **b**) XPS spectra of N80 steel sheets after immersion in 1 mol/L HCl solution containing 500 mg/L Q4-AP-C12 at 363 K for different durations. (**c**) XPS spectra of N80 steel sheet after immersion for 4 h in different corrosive media containing 500 mg/L Q4-AP-C12: 15% HCl solution at 363 and 303 K, 1 mol/L HCl solution at 363 and 303 K. (**d**) Schematic diagram of the corrosion inhibition mechanism of Q4-AP-C12.

intensity. An upward shift in the Fermi level is observed in both cases, indicating reduced surface reactivity. The enhanced C 2*p* DOS in the range of −7.5 to 0 eV for Fe + Q4-AP-C12, ascribable to the grafted alkyl chain, highlights the role of functionalization in reinforcing electronic interactions with the surface. Moreover, global reactivity descriptors, including electronegativity (χ), hardness (η), softness (σ), number of transferred electrons (ΔN), and electrophilicity index (ω), further corroborate the superior inhibition performance of Q4-AP-C12 (Table S6). Q4-AP-C12 exhibits lower electronegativity ($\chi = 5.487$) compared to Q4-AP ($\chi = 5.897$), implying a stronger electron-donating capacity. The higher ΔN value (0.116 vs. 0.080) suggests more favorable electron transfer from Q4-AP-C12 to iron. Concurrently, the reduced electrophilicity index ($\omega = 7.217$ vs. 8.655) aligns well with its enhanced nucleophilic character.

3.7. MD simulations of inhibitor assembly and film stability

To complement the electronic structure calculations, all-atom molecular dynamics (MD) simulations were conducted to investigate the adsorption kinetics and film-forming behavior of Q4-AP-C12 on Fe surfaces in a highly aggressive 15% HCl solution (Fig. 9 and Fig. S5) and 1 mol/L HCl solution (Figs. 6 and 7) environment. The COMPASSII force field was employed for these simulations due to its validated accuracy in describing complex heterogeneous interfaces encompassing organic molecules, aqueous electrolytes, and metal surfaces, which is critical for reliably modeling the self-assembly and stability of the inhibitor film under study (Berrissoul et al., 2022; Deng et al., 2025).

In 15% HCl solution at 363 K, the adsorption behavior exhibits a strong concentration dependence (Fig. 9(a)) and the formation of

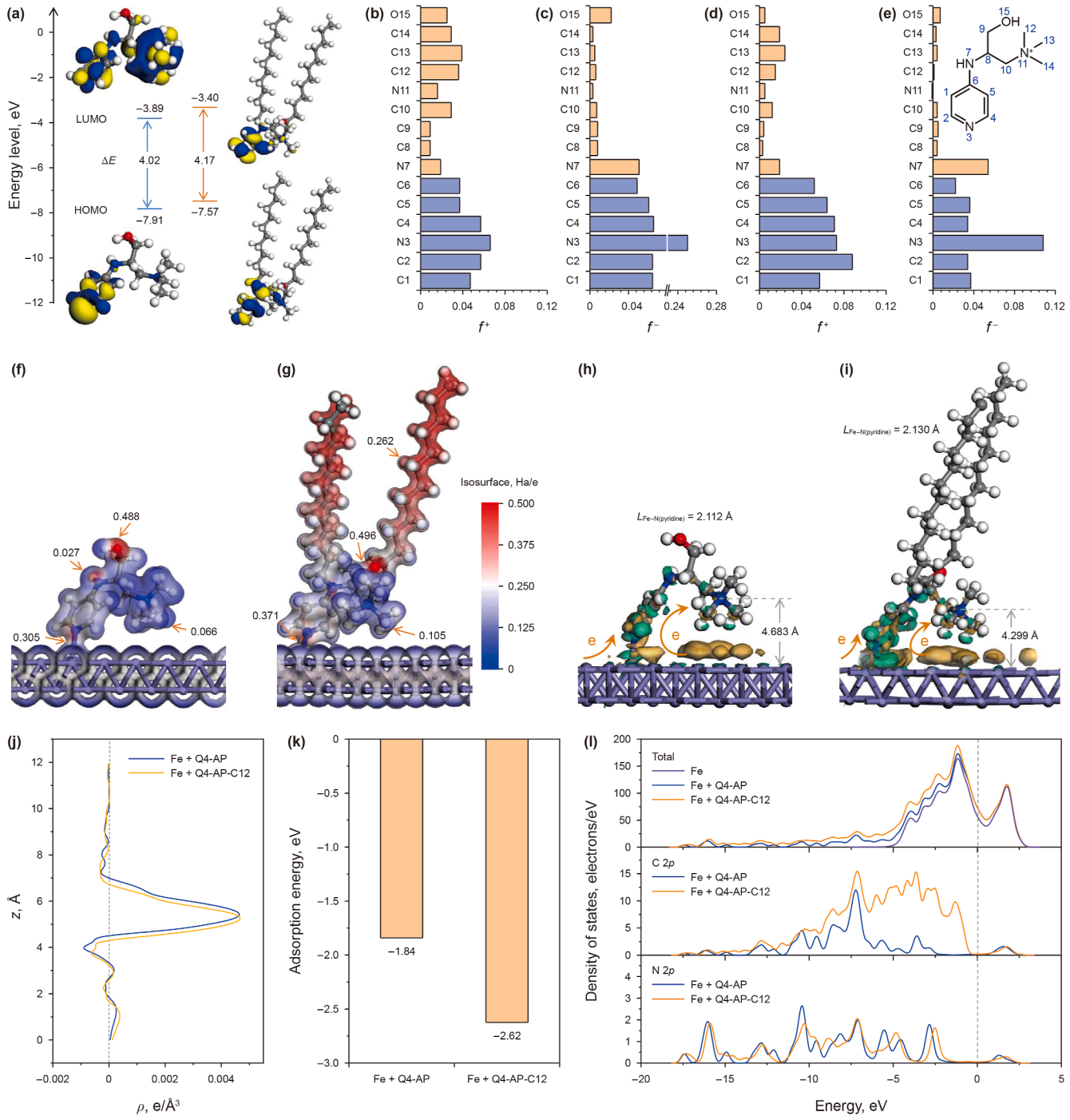

Fig. 8. DFT analysis of the electronic structure and surface interactions. Presented are the frontier molecular orbital (**a**), Fukui function (**b**–**e**), electrostatic potential (**f**, **g**), differential charge density (**h**, **i**), interfacial electron transfer density distribution (**j**), adsorption energy (**k**), and density of states (**l**).

protective bilayer film strictly depends on the concentration of the inhibitor. The specific conditions are summarized in Table S7. With 5 or 15 molecules, monolayer films form with increasing surface coverage. At 25 molecules, a well-defined bilayer structure emerges: The first layer adsorbs directly on the Fe surface, while the second layer is stabilized through hydrophobic interactions between alkyl chains, with polar headgroups oriented toward the solution. Further increasing to 35 molecules leads to micelle formation in the solution phase rather enhanced surface adsorption. Structural analyses through atomic density (Fig. 9(b)), occupied volume fraction (Fig. 9(c)), and free volume fraction (Fig. 9(d)) confirm the formation of a highly compact inhibitor film. Sharp atomic density peaks near the surface, occupied volume fraction approaching 1, and minimal free volume demonstrate excellent molecular packing and film integrity. The film thickness increases with the included molecular number while maintaining structural coherence.

Charge distribution within the film (Fig. 9(e)) reveals a bilayered positive charge accumulation within 5 Å of the Fe surface. The lower charge layer is associated with pyridinic N atoms directly bonded to the surface, while the upper layer corresponds to tertiary/quaternary ammonium groups. This charge configuration

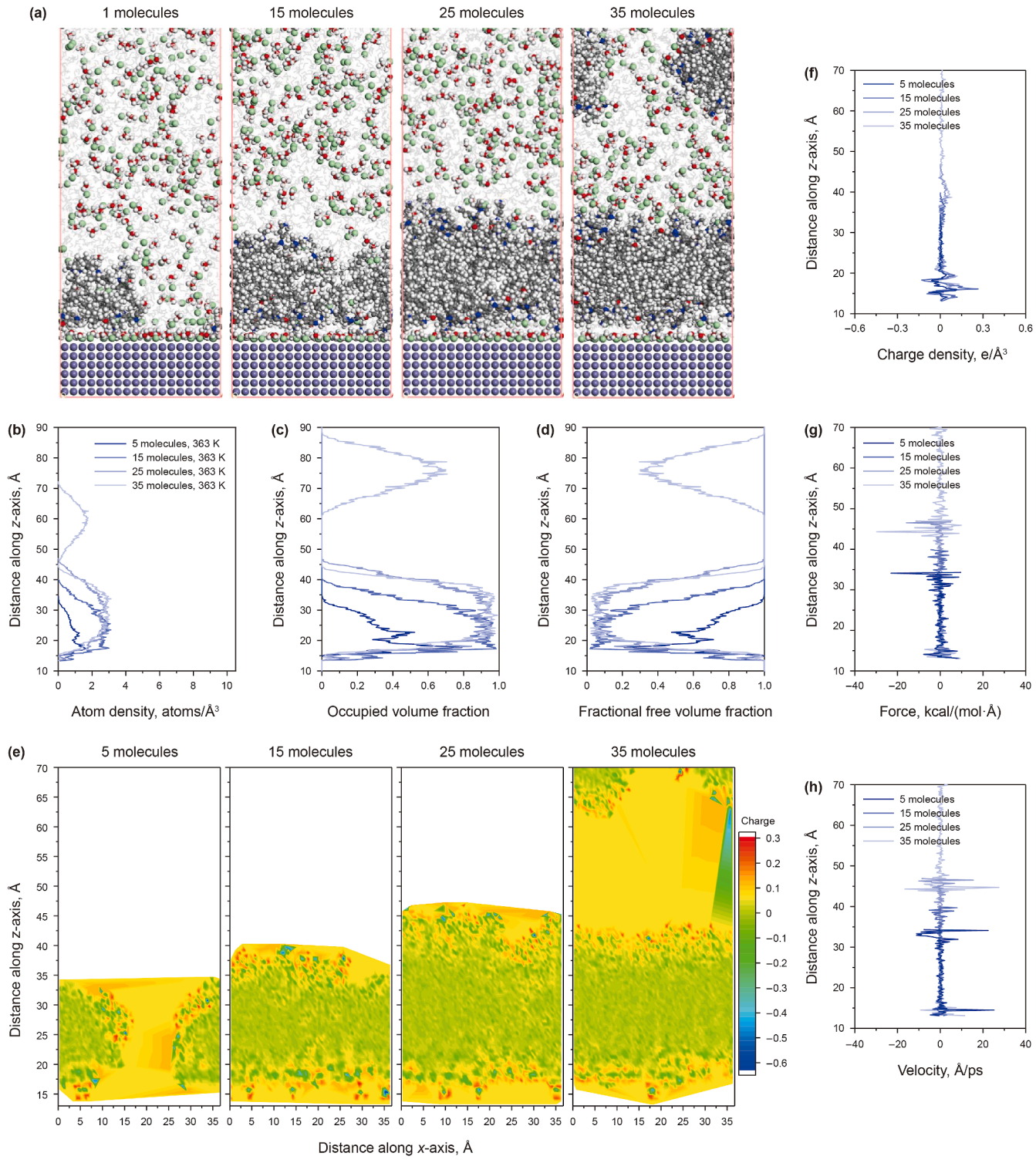

Fig. 9. Molecular modeling of Q4-AP-C12 adsorption on Fe surface in 15% HCl solution at 363 K. Adsorption kinetics and film formation: (**a**) adsorption structures (**a**), (**b**) distributions of atomic density, (**c**) occupied volume fraction, (**d**) free volume fraction. Interfacial electronic and dynamic properties: (**e**) charge distribution morphology, (**f**) distributions of charge density, (**g**) atomic force, (**h**) instantaneous velocity.

enhances interfacial stability and provides electrostatic repulsion against corrosive species. For the 25-molecule system, additional positive charge accumulation at the inhibitor–solution interface further improves corrosion resistance. The distributions of charge density, atomic force, and instantaneous velocity distributions (Fig. 9(f–h)) provide insights into the film's dynamic stability. Two prominent charge density peaks at 14.3 and 16.2 Å (between +0.27 and −0.13 e/Å^2) originate from polar headgroups, while the alkyl chain region shows minimal charge fluctuation (<0.05 e/Å^2). Significant atomic force (−30.0 to +8.6 kcal/(mol·Å)) and velocity (−16.8 to +27.6 Å/ps) fluctuations near the solution interface indicate high dynamic activity in this region.

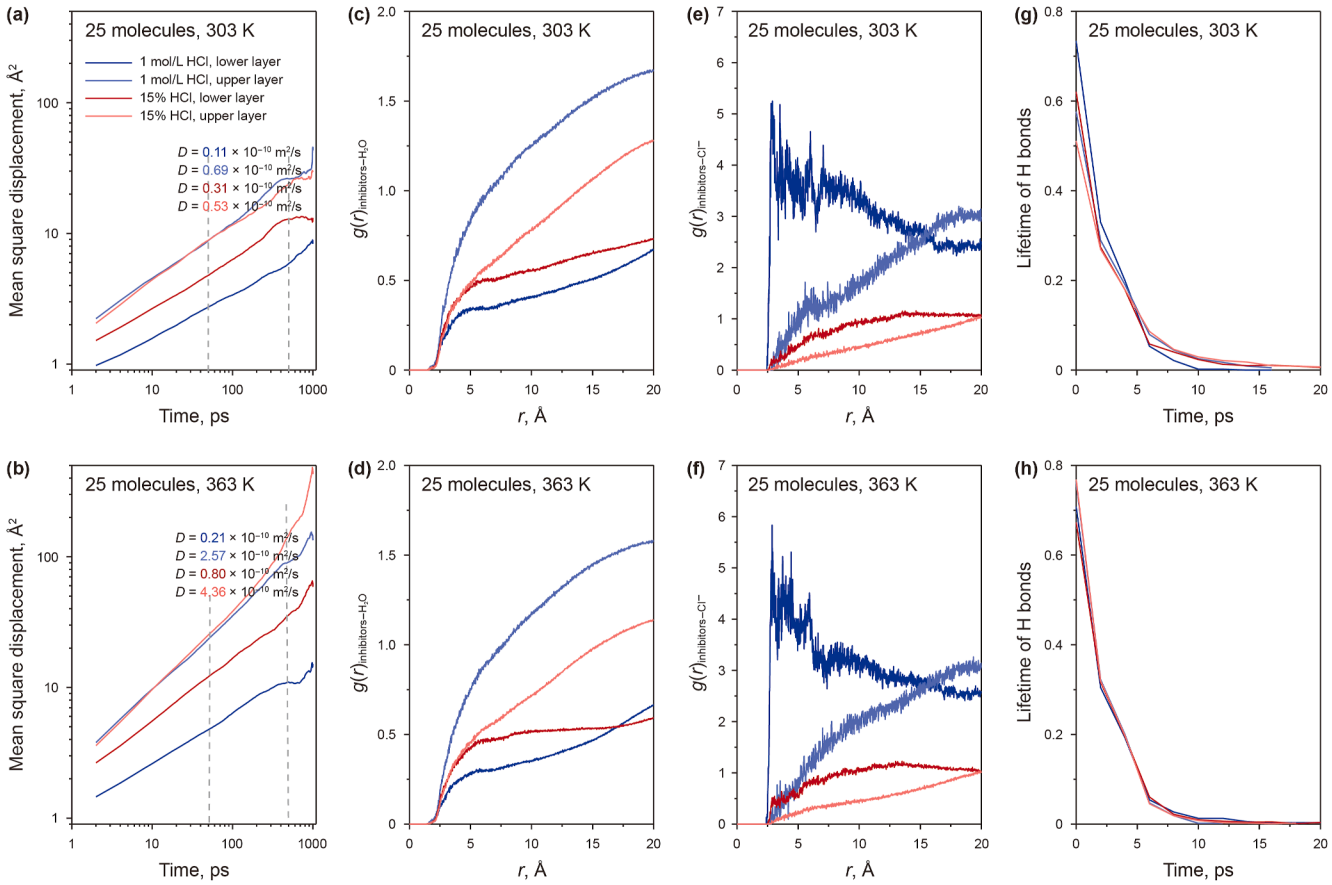

Fig. 10. Molecular-level insights into the lower and upper layers of the 25-molecule system in 1 mol/L and 15% HCl solutions at 303 and 363 K. Profiles of mean square displacements (MSD) (**a**, **b**), radial distribution functions (RDF) (**c**–**f**), and hydrogen bond lifetimes (**g**, **h**).

In contrast, the film formed in 1 mol/L HCl solution demonstrated significantly superior stability and organization. As shown in Figs. S6 and S7, a well-defined and compact bilayer structure emerged at appropriate concentrations, characterized by sharp interfacial density peaks, a high occupied volume fraction, and a distinct bilayered positive charge distribution near the Fe surface. This structured film effectively inhibits the approach of corrosive species, highlighting the strong concentration-dependent efficacy of Q4-AP-C12 in less aggressive acidic environments.

Further layer-resolved analysis of the 25-molecule system through mean square displacement (MSD), radial distribution function (RDF), and hydrogen bond lifetime provides molecular-level insights into bilayer dynamics (Fig. 10). MSD analysis (Fig. 10(a, b)) was specifically utilized to differentiate the translational motion of molecules in the upper and lower layers. The diffusion coefficient (D) was calculated from the slope of the MSD curves within the linear regime of 50–500 ps according to the Einstein relation. Specifically, the lower layer exhibited a significantly lower D (0.11×10^{-10} m^2/s in 1 mol/L HCl at 303 K) compared to the upper layer (0.69×10^{-10} m^2/s), confirming its restricted mobility due to strong surface adsorption. This difference persists across all conditions, though both layers show increased mobility at higher temperatures and acid concentrations. RDF analysis (Fig. 10(c, d)) reveals specific interfacial interactions: The lower layer shows minimal water interaction but strong association with chloride ions, particularly in 1 mol/L HCl solution. These interactions weaken significantly in 15% HCl solution due to competitive ion effects. Hydrogen bond lifetime analysis (Fig. 10(e, f)) shows shorter lifetimes for the lower layer at 303 K, indicating weaker structural stability despite strong adsorption. The upper layer demonstrates longer-lived hydrogen bonds, suggesting better integration with the solution phase. This differentiation diminishes at 363 K, where thermal energy reduces hydrogen bonding contributions to film stability. The above analyses indicate that the bilayer inhibitor film exhibits a stable, tightly bound lower layer providing strong surface attachment, coupled with a dynamic upper layer offering adaptive protection. The structural integrity arises from balanced intermolecular interactions, specific ion associations, and optimized molecular packing. In concentrated acid, competitive adsorption and ion penetration disrupt this delicate balance, leading to increased free volume, charge distribution disruption, and ultimately diminished corrosion protection. These molecular-level insights provide a comprehensive understanding of the inhibition mechanism and its failure under extreme conditions.

4. Conclusions

In this study, a novel corrosion inhibitor, Q4-AP-C12, was designed and synthesized, demonstrating exceptional protective efficacy for oilfield-grade N80 steel under extreme high-temperature and strongly acidic conditions. Comprehensive gravimetric and electrochemical assessments reveal that Q4-AP-C12 has outstanding performance at a dosage of 500 mg/L. It achieves an ultra-low corrosion rate of 0.029 g/(m^2·h) (99.86% inhibition efficiency) in 1 mol/L HCl solution at 303 K and, critically, maintains robust protection (7.29 g/(m^2·h), 99.21% inhibition efficiency) even in 15% HCl solution at 363 K. Multimodal surface

characterization, particularly XPS analysis, confirms the formation of a stable, hydrophobic adsorption film driven by a synergistic mechanism. The distinct N 1*s* peaks at 399.8 eV (N–Fe) and 402.5 eV (N^+–C) provide compelling evidence for the coexistence of coordinative chemisorption and electrostatic physisorption. These experimental findings are strongly corroborated by theoretical calculations. DFT results reveal the molecule's enhanced electron-donating capability (HOMO = −7.57 eV) and high adsorption energy (−2.62 eV), while MD simulations visualize the self-assembly of a compact bilayer structure that effectively impedes the ingress of corrosive species. Furthermore, the molecular design strategy—anchoring hydrophobic alkyl chains to functionalized heterocyclic cations—proves to be highly generalizable and versatile. By modulating the alkyl chain length or the cationic headgroup, inhibitor structures can be precisely tailored for diverse corrosive environments. This versatility positions Q4-AP-C12 as a promising candidate for real-world oilfield acidizing operations, supported by its demonstrated stability under simulated downhole conditions. Future endeavors will focus on field validation, long-term compatibility assessments, and formulation optimization to advance its transition toward cost-effective and environmentally adaptive industrial applications.

CRediT authorship contribution statement

Hui-Ling Su: Writing – original draft, Visualization, Investigation, Formal analysis, Data curation, Conceptualization. **Zhi-Kun Wang:** Writing – review & editing, Supervision, Software, Funding acquisition. **Lei Yu:** Visualization. **Xu-Peng Li:** Methodology, Investigation. **Jia-Qi Feng:** Methodology, Investigation. **Shi-Dong Xia:** Methodology, Investigation. **Zi-Xiao Chen:** Methodology, Formal analysis. **Mian-Tuo Li:** Methodology, Formal analysis. **Si-Yu Liu:** Formal analysis, Data curation. **Yu Fu:** Data curation, Conceptualization. **Jing-Yue Wang:** Visualization, Validation, Software. **Song-Qing Hu:** Writing – review & editing, Supervision, Project administration, Funding acquisition.

Data availability statement

Data will be made available on request.

Declaration of competing interest

The authors declare that they have no known competing financial interests or personal relationships that could have appeared to influence the work reported in this paper.

Acknowledgements

This work was supported by the National Natural Science Foundation of China (52574093, 52204066, 52474020), the Shandong Provincial Natural Science Foundation of China (ZR2025 MS804), the Shandong Province Youth Entrepreneurship Technology Support Program for Higher Education Institutions (2023KJ060), and the Fundamental Research Funds for the Central Universities (23CX06018A).

Supplementary data

Supplementary data to this article can be found online at https://doi.org/10.1016/j.petsci.2026.03.024.

References

Ahmadi, S., Khormali, A., 2024. Optimization of the corrosion inhibition performance of 2-mercaptobenzothiazole for carbon steel in HCl media using response surface methodology. Fuel 357, 129783. https://doi.org/10.1016/j.fuel.2023.129783.

Alawi Al-Sodani, K.A., Baghabra Al-Amoudi, O.S., Maslehuddin, M., et al., 2018. Efficiency of corrosion inhibitors in mitigating corrosion of steel under elevated temperature and chloride concentration. Constr. Build. Mater. 168, 97–112. https://doi.org/10.1016/j.conbuildmat.2017.12.097.

Ansari, K.R., Chauhan, D.S., Quraishi, M.A., et al., 2020. Chitosan Schiff base: An environmentally benign biological macromolecule as a new corrosion inhibitor for oil & gas industries. Int. J. Biol. Macromol. 144, 305–315. https://doi.org/10.1016/j.ijbiomac.2019.12.106.

Berdimurodov, E., Verma, C., Berdimuradov, K., et al., 2022. 8-Hydroxyquinoline is key to the development of corrosion inhibitors: An advanced review. Inorg. Chem. Commun. 144, 109839. https://doi.org/10.1016/j.inoche.2022.109839.

Berrissoul, A., Ouarhach, A., Benhiba, F., et al., 2022. Exploitation of a new green inhibitor against mild steel corrosion in HCl: Experimental, DFT and MD simulation approach. J. Mol. Liq. 349, 118102. https://doi.org/10.1016/j.molliq.2021.118102.

Cui, G.D., Chen, Y.M., Zhang, Q.M., et al., 2023. Three novel dendritic chitosan derivatives for inhibiting acid corrosion of petroleum pipelines. Pet. Sci. 20 (6), 3918–3930. https://doi.org/10.1016/j.petsci.2023.08.010.

Deng, Y.N., Liu, K.Y., Chen, R., et al., 2025. Study of the adsorption behavior of Schiff base-type planar conjugated corrosion inhibitors on metal surfaces using DFT calculations and MD simulations. J. Mol. Struct. 1339, 142423. https://doi.org/10.1016/j.molstruc.2025.142423.

Edwards, A., Osborne, C., Webster, S., et al., 1994. Mechanistic studies of the corrosion inhibitor oleic imidazoline. Corros. Sci. 36, 315–325. https://doi.org/10.1016/0010-938X(94)90160-0.

Fan, S.M., Wang, G., Wang, Y.Z., et al., 2025. Robust corrosion inhibition performance by Mannich-base imidazoline quaternary ammonium salt for mild steel in methanesulfonic acid solution. Colloids Surf., A 725, 137595. https://doi.org/10.1016/j.colsurfa.2025.137595.

Gadioli, A.O., Souza, L.M., Pereira, E.C., et al., 2024. Imidazolium-based ionic liquids as corrosion inhibitors for stainless steel in different corrosive media: An overview. J. Mater. Res. Technol. 29, 803–823. https://doi.org/10.1016/j.jmrt.2024.01.066.

Goni, L.K.M.O., Ali, S.A., Al-Muallem, H.A., et al., 2024. Synthesis of a new quaternary ammonium salt for efficient inhibition of mild steel corrosion in 15 % HCl: Experimental and theoretical studies. Heliyon 10, e38425. https://doi.org/10.1016/j.heliyon.2024.e38425.

Han, T., Guo, J.X., Zhao, Q., et al., 2022. Insights into the multiple applications of modified polyacrylamide as oilfield corrosion inhibitor and water phase tackifier. Pet. Sci. 19 (1), 397–408. https://doi.org/10.1016/j.petsci.2022.01.003.

Haque, J., Srivastava, V., Quraishi, M.A., et al., 2020. Polar group substituted imidazolium zwitterions as eco-friendly corrosion inhibitors for mild steel in acid solution. Corros. Sci. 172, 108665. https://doi.org/10.1016/j.corsci.2020.108665.

Jala, R., Saad, M.A., Sliem, M.H., et al., 2022. An eco-friendly quaternary ammonium salt as a corrosion inhibitor for carbon steel in 5 M HCl solution: Theoretical and experimental investigation. Molecules 27, 6414. https://doi.org/10.3390/molecules27196414.

Jamil, D.M., Aljibori, H.S., Alamiery, A., 2025. Electrochemical analysis of 5-Nitro-2-furaldehyde semicarbazone as a mild steel corrosion inhibitor in corrosive solution: An EIS, adsorption and SEM study. Results. Chem 15, 102193. https://doi.org/10.1016/j.rechem.2025.102193.

Jia, H., Wang, Q., Yan, H., et al., 2024. Investigation of phosphorus-based ionic liquid with long alkyl chain as high-performance corrosion inhibitor with ultralow concentration for mild steel in 1 M HCl solution. J. Mol. Liq. 396, 123946. https://doi.org/10.1016/j.molliq.2023.123946.

Kokalj, A., 2022. Corrosion inhibitors: Physisorbed or chemisorbed? Corros. Sci. 196, 109939. https://doi.org/10.1016/j.corsci.2021.109939.

Lai, X., Hu, J.F., Ruan, T., et al., 2021. Chitosan derivative corrosion inhibitor for aluminum alloy in sodium chloride solution: A green organic/inorganic hybrid. Carbohydr. Polym. 265, 118074. https://doi.org/10.1016/j.carbpol.2021.118074.

Li, D.P., Song, W.W., Zhang, J.P., et al., 2023. Corrosion inhibition mechanism of ultra-high-temperature acidizing corrosion inhibitor for 2205 duplex stainless steel. Materials 16, 2358. https://doi.org/10.3390/ma16062358.

Li, Y.Y., Wang, B.B., Wang, Y., et al., 2025. Beneficial effect of heat input to improve microbial corrosion resistance of welded joint in X80 steel pipeline. J. Mater. Sci. Technol. 223, 217–234. https://doi.org/10.1016/j.jmst.2024.10.034.

Liao, B., Ma, S., Zhang, S., et al., 2023. Fructus cannabis protein extract powder as a green and high effective corrosion inhibitor for Q235 carbon steel in 1 M HCl solution. Int. J. Biol. Macromol. 239, 124358. https://doi.org/10.1016/j.ijbiomac.2023.124358.

Lin, H., Chen, X.R., Luo, Z.M., et al., 2024. Corrosion inhibition properties of corrosion inhibitors to under-deposit corrosion of X65 steel in CO_2 corrosion conditions. Molecules 29, 2611. https://doi.org/10.3390/molecules29112611.

Liu, E.B., Tang, H., Zhang, Y.H., et al., 2023a. Experiment and numerical simulation of distribution law of water-based corrosion inhibitor in natural gas gathering and transportation pipeline. Pet. Sci. 20 (3), 1857–1873. https://doi.org/10.1016/j.petsci.2023.01.015.

Liu, H., Lin, Y.Z., Luo, Q.Y., et al., 2024. Expounding protection mechanisms of ring charge density and ligand number for N-containing heterocyclic as corrosion inhibitors using experimental and calculation. Appl. Surf. Sci. 648, 159069. https://doi.org/10.1016/j.apsusc.2023.159069.

Liu, P., Dai, S.S., Lan, J., et al., 2023b. Corrosion inhibition mechanism of imidazole ionic liquids with high temperature in 20% HCl solution. J. Mol. Model. 29, 29. https://doi.org/10.1007/s00894-022-05436-w.

Liu, Y.F., Chen, L.L., Tang, Y.F., et al., 2022. Synthesis and characterization of nano-SiO_2@octadecylbisimidazoline quaternary ammonium salt used as acidizing corrosion inhibitor. Rev. Adv. Mater. Sci. 61, 186–194. https://doi.org/10.1515/rams-2022-0006.

Luo, F., Yao, P., Zhang, J.L., et al., 2025. Alkyl pyridine ionic liquid as a green corrosion inhibitor for mild steel in acidic medium. RSC Adv. 15, 27369–27387. https://doi.org/10.1039/d5ra04148a.

Luo, X.Y., Li, C., Liu, P.L., et al., 2024. Optimization and evaluation of corrosion inhibitors for N80 steel in sulfamic acid solutions. Int. J. Electrochem. Sci. 19, 100759. https://doi.org/10.1016/j.ijoes.2024.100759.

Madurani, K.A., Firdausi, S., Harmami, H., et al., 2024. Improving inhibition efficiency of 304 stainless steel using an organic extract in acidic and high temperature environment: Experimental and theoretical studies. Appl. Surf. Sci. Adv. 22, 100620. https://doi.org/10.1016/j.apsadv.2024.100620.

Marinescu, M., 2019. Recent advances in the use of benzimidazoles as corrosion inhibitors. BMC Chem. 13, 136. https://doi.org/10.1186/s13065-019-0655-y.

Meng, S.G., Liu, Z.N., Zhao, X.Q., et al., 2021. Efficient corrosion inhibition by sugarcane purple rind extract for carbon steel in HCl solution: Mechanism analyses by experimental and in silico insights. RSC Adv. 11, 31693–31711. https://doi.org/10.1039/D1RA04976C.

Moselhy, M.A., Zaki, E.G., El-Maksoud, S.A., et al., 2022. The role of some cationic surfactants based on thiazine as corrosion inhibitors in petroleum applications: Experimental and theoretical approach. ACS Omega 7, 32014–32025. https://doi.org/10.1021/acsomega.2c02961.

Pisárčik, M., Lukáč, M., Jampílek, J., et al., 2021. Silver nanoparticles stabilized with phosphorus-containing heterocyclic surfactants: Synthesis, physico-chemical properties, and biological activity determination. Nanomaterials 11, 1883. https://doi.org/10.3390/nano11081883.

Qian, S., Cheng, Y., 2019. Synergism of imidazoline and sodium dodecylbenzenesulphonate inhibitors on corrosion inhibition of X52 carbon steel in CO_2-saturated chloride solutions. J. Mol. Liq. 294, 111674. https://doi.org/10.1016/j.molliq.2019.111674.

Ren, S.M., Cui, M.J., Chen, X.Y., et al., 2022. Comparative study on corrosion inhibition of N doped and N, S codoped carbon dots for carbon steel in strong acidic solution. J. Colloid Interface Sci. 628, 384–397. https://doi.org/10.1016/j.jcis.2022.08.070.

Saddik, A.S., Sayed, M., Mohammed, A.K., et al., 2025. Molecular design and performance of emissive amide-containing compounds as corrosion inhibitors: Synthesis, electrochemical evaluation, DFT calculations and molecular dynamics simulations. RSC Adv. 15, 1538415396. https://doi.org/10.1039/D5RA00978B.

Singh, A., Ansari, K.R., Ali, I.H., et al., 2024. Long chain imidazole derivative as a novel corrosion inhibitor for Q235 steel in 15% HCl medium under hydrodynamic condition: Experimental and theoretical examinations. Mater. Chem. Phys. 313, 128798. https://doi.org/10.1016/j.matchemphys.2023.128798.

Sun, X., Xu, H.X., Cao, Y.J., et al., 2025. Progress in the design of molecular structure of amino acid corrosion inhibitors based on molecular orbital theory and their mechanisms: A review. J. Mol. Liq. 427, 127374. https://doi.org/10.1016/j.molliq.2025.127374.

Tang, M., Deng, S.D., Du, G.B., et al., 2023. Mikania micrantha extract/KI blend as a novel synergistic inhibitor for steel corrosion in concentrated H_3PO_4 solution. Ind. Crop. Prod. 193, 116237. https://doi.org/10.1016/j.indcrop.2023.116237.

Tang, M., Deng, S.D., Xu, D.K., et al., 2025. Novel quaternary ammonium Gemini surfactant as a highly efficient inhibitor for the corrosion of steel in HCl and H_2SO_4 solutions. J. Mater. Sci. Technol. 223, 287–307. https://doi.org/10.1016/j.jmst.2024.10.038.

Verma, C., Dubey, S., Ebenso, E.E., et al., 2025. Polypyridyl-based bridging corrosion inhibitors: A critical review on interface and ligands properties. Adv. Colloid Interface Sci. 342, 103534. https://doi.org/10.1016/j.cis.2025.103534.

Verma, C., Rhee, K.Y., Quraishi, M.A., et al., 2020. Pyridine based N-heterocyclic compounds as aqueous phase corrosion inhibitors: A review. J. Taiwan Inst. Chem. Eng. 117, 265–277. https://doi.org/10.1016/j.jtice.2020.12.011.

Wang, G., Wang, Y.Z., Fan, S.M., et al., 2026. Elevated-temperature corrosion inhibition of mild steel in sulfuric acid by coupled effects of imidazoline-type inhibitor and thiourea derivatives. J. Mater. Sci. Technol. 240, 233–249. https://doi.org/10.1016/j.jmst.2025.05.004.

Wang, J., An, L., Wang, J., et al., 2023. Frontiers and advances in N-heterocycle compounds as corrosion inhibitors in acid medium: Recent advances. Adv. Colloid Interface Sci. 321, 103031. https://doi.org/10.1016/j.cis.2023.103031.

Wang, J., Wang, Y.F., Yang, Z., et al., 2024. Synthesis of a novel fused heterocyclic quaternary ammonium salt and its performance in ultra-low dosage as acidizing corrosion inhibitor. J. Mol. Struct. 1303, 137571. https://doi.org/10.1016/j.molstruc.2024.137571.

Wang, Q., Zhou, X.B., Ma, Q., et al., 2022. Selected corrosion of X80 pipeline steel welded joints induced by Desulfovibrio desulfuricans. Corros. Sci. 202, 110313. https://doi.org/10.1016/j.corsci.2022.110313.

Wazzan, N., Obot, I.B., Fagieh, T.M., 2022. The role of some triazoles on the corrosion inhibition of C1020 steel and copper in a desalination descaling solution. Desalination 527, 115551. https://doi.org/10.1016/j.desal.2022.115551.

Wen, Y., Ma, X.M., Cai, Y.X., et al., 2023. Corrosion inhibition mechanism of vitamins on steel bars in chloride environments: Experimental analysis and quantum chemical calculation. Constr. Build. Mater. 406, 133424. https://doi.org/10.1016/j.conbuildmat.2023.133424.

Xhanari, K., Farruku, M., Berisha, A., et al., 2025. Experimental and theoretical evaluation of the corrosion inhibition performance of two benzimidazole derivatives for low carbon steel in acidic solution. RSC Adv. 15, 24815–24830. https://doi.org/10.1039/D5RA02749G.

Ye, Y.W., Yang, D.P., Chen, H., 2019. A green and effective corrosion inhibitor of functionalized carbon dots. J. Mater. Sci. Technol. 35, 2243–2253. https://doi.org/10.1016/j.jmst.2019.05.045.

Zhang, F., Liu, S., Zhang, X., et al., 2023a. Research on 1,10-phenanthroline quaternary ammonium salt composite corrosion inhibitors for oilfield acidizing at high temperatures and high HCl concentrations. Geoenergy Sci. Eng. 225, 211663. https://doi.org/10.1016/j.geoen.2023.211663.

Zhang, L., Zhang, A., Zhou, S.S., et al., 2023b. Study of okra pectin prepared by sweeping frequency ultrasound/freeze-thaw pretreatment on corrosion inhibition of ANSI 304 stainless steel in acidic environment. Int. J. Biol. Macromol. 253, 126587. https://doi.org/10.1016/j.ijbiomac.2023.126587.

Zhao, C., Xiang, W.J., Zhang, C.Y., et al., 2024. Experimental and theoretical studies on long alkyl chain-bearing dibenzotriazole ionic liquids as eco-friendly corrosion inhibitors in aqueous hydrochloride acid. Langmuir 40, 15232–15243. https://doi.org/10.1021/acs.langmuir.4c01722.

Zhong, Z., Wei, B.X., Wang, Z.S., et al., 2026. Microbiologically assisted stress corrosion cracking of X80 pipeline steel welded joint under cathodic protection. Acta Mater. 303, 121722. https://doi.org/10.1016/j.actamat.2025.121722.